Giant Band Degeneracy *via* Orbital Engineering Enhances Thermoelectric Performance from $Sb_2Si_2Te_6$ to $Sc_2Si_2Te_6$

Wenzhen Dou, Kieran B. Spooner, Seán R. Kavanagh, MiaoZhou* and David O. Scanlon**

W. Dou, Prof. M. Zhou

School of Physics, Beihang University, Beijing 100191, China

W. Dou, K. B. Spooner, S. R. Kavanagh, Prof. D. O. Scanlon

Department of Chemistry, University College London, London WC1H 0AJ, United Kingdom

K. B. Spooner, Prof. D. O. Scanlon

School of Chemistry, University of Birmingham, Birmingham B15 2TT, United Kingdom

S. R. Kavanagh

Department of Materials, Imperial College London, London SW7 2AZ, United Kingdom

K. B. Spooner, S. R. Kavanagh, Prof. D. O. Scanlon

Thomas Young Centre, University College London, London WC1E 6BT, United Kingdom

W. Dou, Prof. M. Zhou

Collaborative Centre for Physics and Chemistry, Institute of International Innovation, Beihang University, Hangzhou 311115, China

Prof. M. Zhou

Tianmushan Laboratory, Hangzhou 310023, China

***E-mail:** s.kavanagh19@imperial.ac.uk (S.R.K.); mzhou@buaa.edu.cn (M.Z.); d.o.scanlon@bham.ac.uk (D.O.S.)

Abstract

The complex interrelationships among thermoelectric parameters mean that a *priori* design of high-performing materials is difficult. However, band engineering can allow the power factor to be optimized through enhancement of the Seebeck coefficient. Herein, using layered $Sb_2Si_2Te_6$ and $Sc_2Si_2Te_6$ as model systems, we comprehensively investigate and compare their thermoelectric properties by employing density functional theory combined with semiclassical Boltzmann transport theory. Our simulations reveal that $Sb_2Si_2Te_6$ exhibits superior electrical conductivity compared to $Sc_2Si_2Te_6$ due to lower scattering rates and more pronounced band dispersion. Remarkably, despite $Sb_2Si_2Te_6$ exhibiting a lower lattice thermal conductivity, the introduction of Sc-*d* orbitals dramatically increases conduction band degeneracy in $Sc_2Si_2Te_6$, yielding a significantly improved Seebeck coefficient relative to $Sb_2Si_2Te_6$. As a result, $Sc_2Si_2Te_6$ is predicted to achieve an extraordinary dimensionless figure of merit (*ZT)* of 3.51 at 1000 K, which significantly surpasses the predicted maximum *ZT* of 2.76 for $Sb_2Si_2Te_6$ at 900 K. This work suggests that engineering band degeneracy through compositional variation is an effective strategy for improving the thermoelectric performance of layered materials.

Keywords: layered thermoelectric materials, band degeneracy, enhanced Seebeck coefficient, first-principles calculation, momentum relaxation time approximation

Introduction

With the development of electronics and ever-increasing demand for sustainable and versatile energy harvesting, thermoelectrics have become the subject of rapidly growing interest because they can directly transform thermal energy into valuable electrical power.[1] The efficiency of thermoelectric materials is quantified by the dimensionless figure of merit ZT, defined as $ZT = S^2\sigma T/\kappa$, where S is the Seebeck coefficient, σ represents the electrical conductivity, and T denotes the absolute temperature. The thermal conductivity κ includes both lattice thermal conductivity κ_l and the electronic thermal conductivity κ_e. An ideal thermoelectric material should simultaneously exhibit high electrical conductivity to minimize internal energy loss, a high Seebeck coefficient for generating high voltage, and low thermal conductivity to maintain the temperature gradient. Motivated by these design principles, considerable efforts in the past decade have been devoted to exploring potential candidates that inherently possess the crucial attributes required for thermoelectric applications.[2] Among the rapidly growing class of thermoelectric materials, layered compounds have shown advantages due to their unique crystal structure characterized by strong intralayer and weak interlayer bonds.[3] Firstly, their strong discrepancy in chemical bonding strength is believed to induce partially-localized low-frequency phonon modes, low phonon group velocities, and large anharmonicity — all favourable for achieving low lattice thermal conductivity.[4] Moreover, the low-dimensional structure translates to reduced dimensionality in the electrical transport properties, which can benefit thermoelectric performance.[5] Furthermore, the anisotropic behaviour of electron and phonon transport in these layered systems provides an excellent opportunity to disentangle the interconnected thermoelectric parameters, especially when thermoelectric conversion occurs along the desired crystal direction within a single crystal.[6]

Within the layered compounds, the $A_2B_2Q_6$ family (A = In, Cr, Bi, Sb or Sc; B = Si, Ge, and Q = Se, Te) has been intensively explored[7] and some compounds show intriguing magnetic and magnetoelectric properties, such as pressure-driven spin-

crossover and long-range ferromagnetic order.[7d, 7e] Interestingly, compounds based on A = Cr, Sb, In, and Bi are also reported to be promising candidates for thermoelectric applications.[3a, 7b, 8] In particular, $Sb_2Si_2Te_6$ has been the focus of interest due to its remarkable thermoelectric properties.[3a, 9] $Sb_2Si_2Te_6$ adopts a layered two-dimensional structure composed of Sb^{3+} cations and $[Si_2Te_6]^{6-}$ units, resembling the $Fe_2P_2Se_6$ structure type. Owing to a low phonon group velocity and strong anharmonicity, $Sb_2Si_2Te_6$ exhibits a relatively low thermal conductivity, approximately 1.3 W m^{-1} K^{-1} at room temperature, decreasing to 0.5 W m^{-1} K^{-1} at 823 K.[3a] Consequently, $Sb_2Si_2Te_6$ achieves an impressive *ZT* of 1.08 at 823 K.[3a] Additionally, by constructing a cellular nanostructure through the deposition of a thin layer of Si_2Te_3 onto $Sb_2Si_2Te_6$ grains, the peak *ZT* at 823 K can be improved to 1.65 in the $Sb_2Si_2Te_6/Si_2Te_3$ cellular network.[3a] Nevertheless, the average power factor (PF) of $Sb_2Si_2Te_6$ — approximately 10 μW cm^{-1} K^{-2} within the temperature range of 400–823 K — lags behind that of conventional Pb-based thermoelectric materials (~30 μW cm^{-1} K^{-2} for p-type PbTe and ~20 μW cm^{-1} K^{-2} for n-type PbTe).[10] As a result, it is highly desirable to enhance the PF and, by extension, the overall thermoelectric performance of $Sb_2Si_2Te_6$-based thermoelectric devices.

Band engineering strategies are widely employed to improve the thermoelectric performance of materials.[11] Band degeneracy, in particular, can enhance the PF by increasing the Seebeck coefficient and thus the ultimate thermoelectric performance.[12] Band or valley degeneracy refers to the case where multiple bands have identical (degenerate) or closely matching within a few k_BT (effectively degenerate) energies. This can happen when *different bands* have minimal (or no) energy difference at the band edge (termed orbital degeneracy) and/or when multiple pockets of the *same bands* in the Brillouin zone are (effectively) degenerate, often due to symmetry equivalence *via* the combination of crystal and orbital symmetries (termed k-point degeneracy). Recently, Wang et al. reported a 22 % improvement in the *ZT* due to enhanced band degeneracy upon substituting *p*-valent Bi in BiCuOSe with *d*-valent La, predicting a *ZT* value of 1.46 for *n*-type LaCuOSe.[13] We posit that a similar band-degeneracy induced

enhancement of the thermoelectric performance may be achievable in the $A_2B_2Q_6$ family by replacing *p*-valent Sb with a *d*-valent cation. Several members of the $A_2B_2Q_6$ family have been experimentally reported thus far, including $Sc_2Si_2Te_6$ in 2022[7a] — however, the thermoelectric properties were not investigated.

In this work, we investigate the effects on band degeneracy and thermoelectric performance by modifying the conduction band orbital character in this crystal family, shifting from a Sb-*p* derived CBM in $Sb_2Si_2Te_6$ to a Sc-*d* CBM in $Sc_2Si_2Te_6$. $Sc_2Si_2Te_6$ shares an identical stacking fault pattern with $Sb_2Si_2Te_6$, and crystallizes in the same rhombohedral symmetry (space group $R\bar{3}$) with a single distinct crystallographic position each for Sc, Si and Te as revealed experimentally by high-resolution transmission electron microscopy and diffraction patterns.[7a] We systematically investigated the thermal and electrical transport properties in layered $Sb_2Si_2Te_6$ and $Sc_2Si_2Te_6$ by solving the Boltzmann transport equation based on first-principles calculations, revealing a significant enhancement of band degeneracy and, consequently, the Seebeck coefficient in $Sc_2Si_2Te_6$ compared to $Sb_2Si_2Te_6$. We predict n-type $Sc_2Si_2Te_6$ to achieve an optimal *ZT* of 3.51 at 1000 K, surpassing the maximum *ZT* of 2.76 obtained for p-type $Sb_2Si_2Te_6$ by 27 %. These findings demonstrate that $Sc_2Si_2Te_6$ presents a competitive alternative to $Sb_2Si_2Te_6$, highlighting the validity of band degeneracy engineering in optimizing the PF and thermoelectric performance.

Results and Discussion

Equilibrium geometry and electronic structure

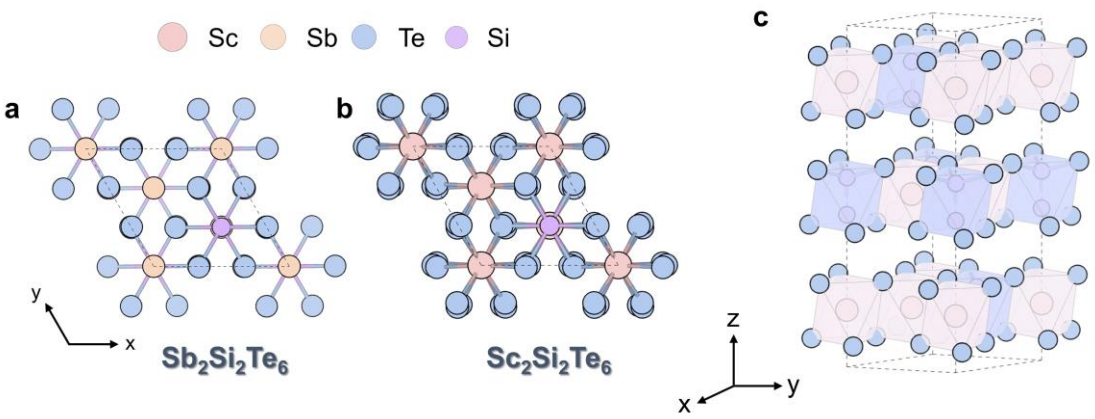

Figure 1 Top view of the crystal structure for (a) $Sb_2Si_2Te_6$ and (b) $Sc_2Si_2Te_6$. The

conventional unit cell is indicated by grey dashed lines. (c) Side view of $Sc_2Si_2Te_6$. There is a slight asymmetric distortion of the octahedra in $Sc_2Si_2Te_6$. The atom colours are Sb: orange, Sc: pink, Si: purple, and Te: blue.

Both $Sb_2Si_2Te_6$ (Figure 1a) and $Sc_2Si_2Te_6$ (Figure 1b) exhibit rhombohedral symmetry (space group $R\bar{3}$, No. 148) and consist of ABC-stacked slabs of $(Sb/Sc)_2Si_2Te_6$, where Sb (Sc) atoms and Si–Si dumbbells are arranged within the slabs (Figure 1c). Table 1 presents the lattice parameters of the conventional unit cell, optimized using both PBEsol and HSE06 with the D3 dispersion correction. The calculated lattice constants for $Sb_2Si_2Te_6$ and $Sc_2Si_2Te_6$ agree well with the experimental measurements[3a, 7a] with HSE06+D3 showing improved agreement, though with a slight underestimation of the interlayer spacing as expected when neglecting temperature effects.[14] Compared to $Sb_2Si_2Te_6$, $Sc_2Si_2Te_6$ exhibits a slight asymmetric distortion of the octahedra, with shorter Sc–Te bond lengths due to the smaller ionic radius of Sc but larger interlayer spacing.

Table 1 Calculated crystal structure information of $Sb_2Si_2Te_6$ and $Sc_2Si_2Te_6$. The % differences to the experimental structures are given in parentheses.[3a, 7a] d_{layer} is the interlayer distance.

Functional	Compound	a (Å)	c (Å)	Sb/Sc–Te (Å)	d_{layer} (Å)
PBEsol+D3	$Sb_2Si_2Te_6$	7.07 (–1.4 %)	20.10 (–5 %)	3.05	2.78
	$Sc_2Si_2Te_6$	6.85 (–2 %)	20.16 (–5 %)	2.90	2.99
HSE06+D3	$Sb_2Si_2Te_6$	7.08 (–1.2 %)	20.78 (–2 %)	3.05	3.05
	$Sc_2Si_2Te_6$	6.91 (–1.2 %)	20.81 (–2 %)	2.93	3.22

Using HSE06+SOC with the *doped* package,[15] the stability region (chemical potential limits) of $Sc_2Si_2Te_6$ in the Sc–Si–Te chemical space was computed (Figure S1), showing it to be thermodynamically stable with a relatively large stability window, suggesting ready synthesizability as witnessed experimentally.[7a]

Figure 2 displays the calculated electronic band structures and DOS of $Sb_2Si_2Te_6$ and $Sc_2Si_2Te_6$ using HSE06+SOC. The difference in A-site cations markedly affects the band structure. $Sb_2Si_2Te_6$ exhibits a direct band gap of 0.48 eV, with both the CBM and VBM located at the Z point and this value is close to the experimental optical gap (~

0.6 eV).[3a] In contrast, $Sc_2Si_2Te_6$ exhibits an indirect band gap of 0.92 eV, where the VBM is located at the Γ point and the CBM is at the Σ point along the L–B path in reciprocal space. This is not a high-symmetry k-point, resulting in significantly increased k-point degeneracy at the conduction band edge.[11b] $Sb_2Si_2Te_6$ has high electronic band dispersion, which will yield small carrier effective masses and higher carrier mobility. As indicated by the accompanying DOS plots in Figure 2, the CBM is composed of Sb-*5p* and Te-*5p* orbitals in $Sb_2Si_2Te_6$ and Sc-*3d* orbitals in $Sc_2Si_2Te_6$, while the VBM mainly derives from Te-5*p* orbitals. In $Sb_2Si_2Te_6$ there is a slight contribution to the VBM from Sb-5*s* orbitals while there is minimal hybridization with Sc-3*d* orbitals at the VBM in $Sc_2Si_2Te_6$, which modifies the Te-*p* valence band edge. Consequently, the VBM in $Sc_2Si_2Te_6$ is located at Γ (rather than Z), is doubly (rather than singly) degenerate and exhibits reduced band dispersion. As expected due to the presence of heavy elements Te and (to a lesser extent) Sb, spin–orbit coupling (SOC) is found to significantly reduce the band gaps of these compounds, contributing VBM upshifts of 0.2–0.3 eV (Figure S2).

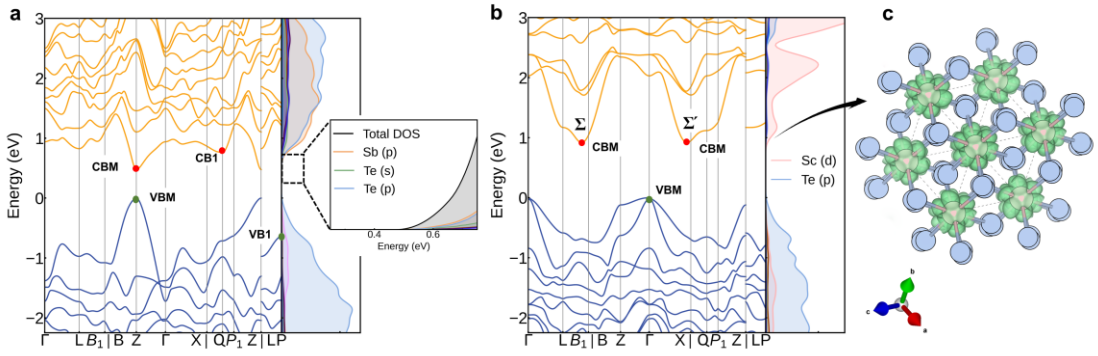

Figure 2 Calculated electronic band structures and orbital-projected DOS of (a) $Sb_2Si_2Te_6$ and (b) $Sc_2Si_2Te_6$ using HSE06+SOC, along the high-symmetry k-point path for rhombohedral crystals within the Setyawan & Curtarolo convention.[16] The VBM is set to zero. (c) Charge density isosurface of the $Sc_2Si_2Te_6$ CBM state. The isosurface level is set to 0.02eV/Å^3.

It is noteworthy that $Sb_2Si_2Te_6$ exhibits an energy difference of 0.3 eV between the lowest two conduction band valleys (i.e., E_{CB1}–E_{CBM}) and 0.6 eV between the highest two valence band valleys (i.e., E_{VBM}–E_{VB1}). In contrast, $Sc_2Si_2Te_6$ features two identical

CBM valleys (Σ and Σ′) and a doubly orbital-degenerate Te-*p* VBM. Reduced energy differences between adjacent bands near the Fermi level result in increased effective band degeneracy, thus yielding a higher effective DOS in $Sc_2Si_2Te_6$. As a result of the differing locations of the band extrema in $Sb_2Si_2Te_6$ (both VBM and CBM at Z) and $Sc_2Si_2Te_6$ (VBM at Γ and CBM at Σ), there is a significant difference in their k-point degeneracy. For the VBM, the k-point degeneracy is 1 in both systems. However, the CBM in $Sc_2Si_2Te_6$ displays a notably higher k-point degeneracy of 18, as opposed to the value of 1 in $Sb_2Si_2Te_6$. The band-decomposed charge density of the CBM in $Sc_2Si_2Te_6$ can provide insights into the high band degeneracy, exhibiting hexagonal symmetry (6-fold degenerate) along the in-plane direction, as seen in Figure 2c. Due to the crystal symmetry (hexagonal ABC stacking) and orbital symmetry (hybridized $d_{x^2-y^2}$, d_{xz} and d_{z^2}, Figures 2 and S3), there are two other diagonal cross-plane directions (corresponding to the Σ′ k-point) which are also degenerate and exhibit hexagonal (6-fold) symmetry. Therefore, the total k-point degeneracy of the CBM state in $Sc_2Si_2Te_6$ is 18. To further elucidate this point, the Fermi surfaces are plotted at 0.1 eV above (below) the CBM (VBM) using the IFermi package[17] (Figure 3). Due to the symmetry of the Brillouin zone, there is two half electron (hole) pockets at the Z point for $Sb_2Si_2Te_6$ and thus the k-point degeneracy is 1 for both VBM and CBM (Figure 3a). For $Sc_2Si_2Te_6$, the VBM is at Γ, and an isolated full–hole pocket is generated in the centre of the Brillouin zone — again corresponding to a k-point degeneracy of 1. Meanwhile, six relatively flat electron pockets appear close to the edges of the Brillouin zone for the CBM (Figure 3b). These electron pockets show significant anisotropy, being mostly flat along the *z* (cross-plane) direction but relatively dispersed along the horizontal direction. Using a dense interpolated k-point mesh and setting the Fermi surface energy to just 3 meV above CBM, we see that there are in fact three degenerate elliptical electron pockets within each of the six larger pockets observed with the higher Fermi level — corresponding to the total effective k-point degeneracy of 18 for the CBM in $Sc_2Si_2Te_6$ (Figure 3c). From this analysis, we also determine the CBM k-point coordinates to be Σ = (0.5, 0.16, −0.16). The increased k-point degeneracy in $Sc_2Si_2Te_6$

thus yields a giant band degeneracy, dramatically enhancing the DOS effective mass. In addition, the DOS effective masses closely depend on the carrier effective masses, summarized in Table 2. $Sc_2Si_2Te_6$ displays larger and more anisotropic effective masses for both electrons and holes compared to $Sb_2Si_2Te_6$, as expected, which is also represented by the smaller Fermi velocities of $Sc_2Si_2Te_6$ compared to $Sb_2Si_2Te_6$ (Figure 3). Therefore, the heightened band degeneracy, combined with increased carrier effective masses, is anticipated to result in a significantly higher Seebeck coefficient for $Sc_2Si_2Te_6$.

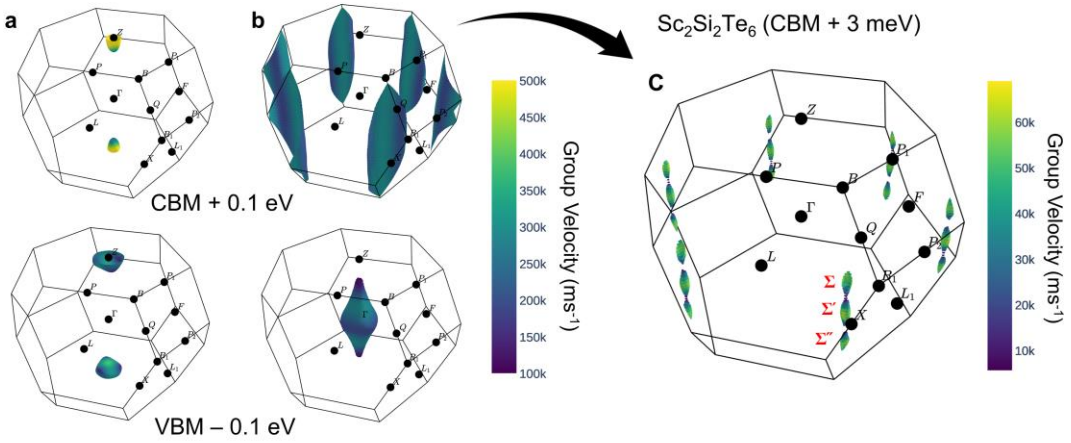

Figure 3. Fermi surface of (a) $Sb_2Si_2Te_6$ and (b) $Sc_2Si_2Te_6$ plotted at 0.1 eV below CBM and above VBM, respectively. (c) The iso-energy Fermi surface is 3 meV above the CBM for $Sc_2Si_2Te_6$. The different colours represent the magnitude of carrier group velocities.

Table 2. Hole and electron effective masses (m_e) of $Sb_2Si_2Te_6$ and $Sc_2Si_2Te_6$ were calculated using parabolic fitting in sumo with the HSE06+SOC functional. The corresponding k-point path is given in parentheses.

System	Hole (m_e)	Electron (m_e)
$Sb_2Si_2Te_6$	0.17 (Z−X) 0.28 (Z−B) 0.28 (Z−Q)	0.29 (Z−X) 0.09 (Z−B) 0.09 (Z−Q)
$Sc_2Si_2Te_6$	0.32 (L−B_1) 0.33 (Γ−X) 3.67 (Γ−B)	0.43 (Σ−B_1) 0.32 (Σ−Γ)

Band alignment

The band alignment of $Sb_2Si_2Te_6$ and $Sc_2Si_2Te_6$ is calculated using the core–level alignment approach (see Supplementary Information for more details).[18] The results are depicted in Figure 4 together with the band alignment of several other high-performance thermoelectric materials. The electron affinities (EA) and ionization

potentials (IP) can provide an indication of the propensity to p- or n-type dopability. Compared to bipolar-dopable PbTe, the IP of $Sb_2Si_2Te_6$ is smaller (due to the anti-bonding Sb-*s* – Te-*p* interaction at the VBM), while that of $Sc_2Si_2Te_6$ is larger, indicating the formation of p-type defects may be more likely for $Sb_2Si_2Te_6$. Indeed, $Sb_2Si_2Te_6$ exhibits strong p-type behaviour experimentally, which is attributed to Sb vacancies.[3a] The EA of $Sc_2Si_2Te_6$ is analogous to that of PbTe, n-type $Y_2Ti_2O_5S_2$ and $BaSnO_3$, while that of $Sb_2Si_2Te_6$ is smaller, suggesting that $Sc_2Si_2Te_6$ may favour n-type doping.

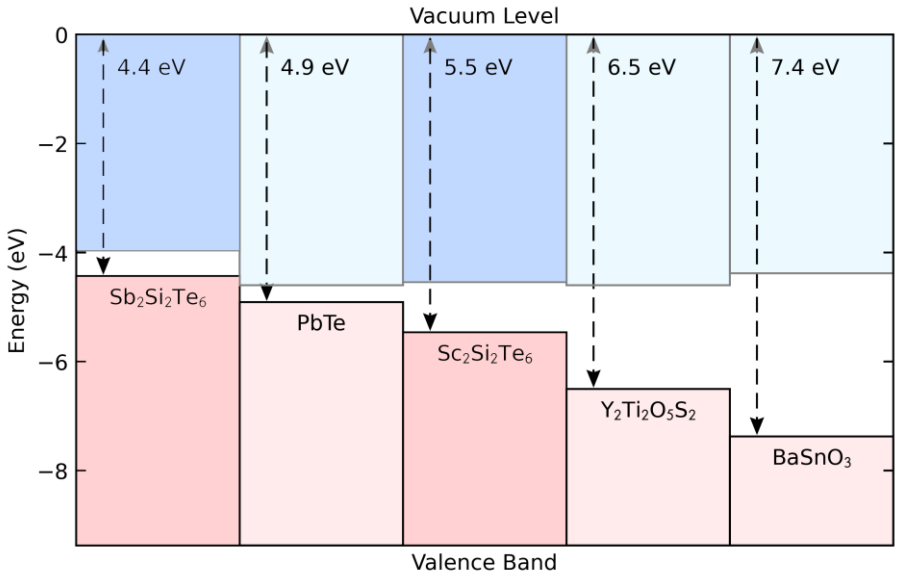

Figure 4 Band alignment of $Sb_2Si_2Te_6$ and $Sc_2Si_2Te_6$ calculated in this study and compared to the band alignments of bipolar PbTe,[19] n-type $Y_2Ti_2O_5S_2$[20] and $BaSnO_3$.[21] Ionisation potential (IP) is annotated.

Electronic transport properties

Using the calculated electronic (Figure 2), phonon (Figure S8) and electron–phonon properties from DFT, the carrier mobilities were computed using the Boltzmann transport equations as implemented in the AMSET package (see Methods and Supplementary Information).[22] The individual scattering mechanisms are plotted as functions of temperature, carrier concentration and electronic energy in Figures S4 and S5. As expected, the dominant mobility-limiting scattering mechanism varies between polar-optical phonon (POP), ionised impurity (IMP) or acoustic deformation potential (ADP) scattering, depending on the doping/carrier concentration and temperature.

Under temperature and doping concentrations which maximise *ZT* (shown later), carrier–phonon scattering dominates for $Sb_2Si_2Te_6$ — primarily due to the lower energy phonon modes from the heavier Sb atoms (Figure S8) — with POP scattering dominant under *p*-type doping and ADP scattering under *n*-type doping. For $Sc_2Si_2Te_6$ on the other hand, IMP scattering dominates under *ZT*-optimised conditions. The resultant electronic transport properties for n-type and p-type doping across a range of carrier concentrations and temperatures are shown in Figures 5 and 6, respectively. As expected, we witness decreases in electrical conductivity with increasing temperature, however the effect is relatively minor for high carrier concentrations due to the dominance of (mostly) temperature-independent impurity scattering over carrier–phonon scattering in these regimes. For *n*-type $Sb_2Si_2Te_6$, the temperature dependence is stronger due to greater carrier–phonon interactions for this case. Overall, $Sb_2Si_2Te_6$ exhibits higher electrical conductivity than $Sc_2Si_2Te_6$ under both *n* and (particularly) *p*-type conditions due to the lower carrier effective masses (Figure 2, Table 2) and scattering rates (Figures S4 and S5). The enhanced band degeneracy in $Sc_2Si_2Te_6$ may also increase the rate of inter-valley scattering, contributing to a decrease in carrier mobility.[11b] As expected from the Wiedemann–Franz law ($\kappa_e = L\sigma T$, where L is the Lorenz number and T is temperature), the trends in electronic thermal conductivity (κ_e) mostly follow those of electrical conductivity (σ).

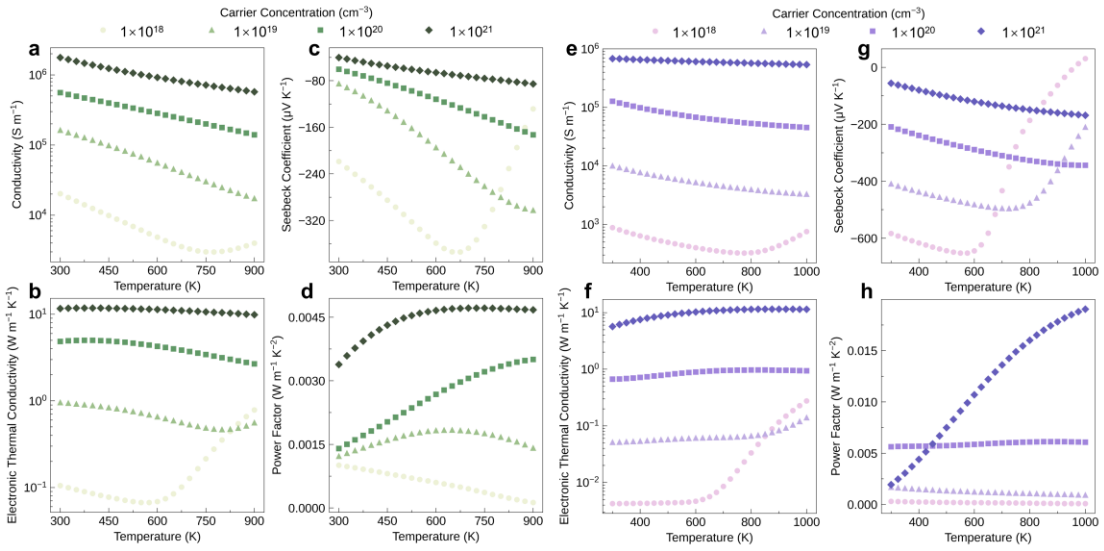

Figure 5 The calculated electronic transport properties as a function of temperature for

n-type (a, b, c, and d) $Sb_2Si_2Te_6$ and (e, f, g, and h) $Sc_2Si_2Te_6$ with four different carrier concentrations. $Sb_2Si_2Te_6$ and $Sc_2Si_2Te_6$ have demonstrated thermal stability up to 920 K and 1023 K,[3a, 7a] respectively, and so these ranges are used in our analysis.

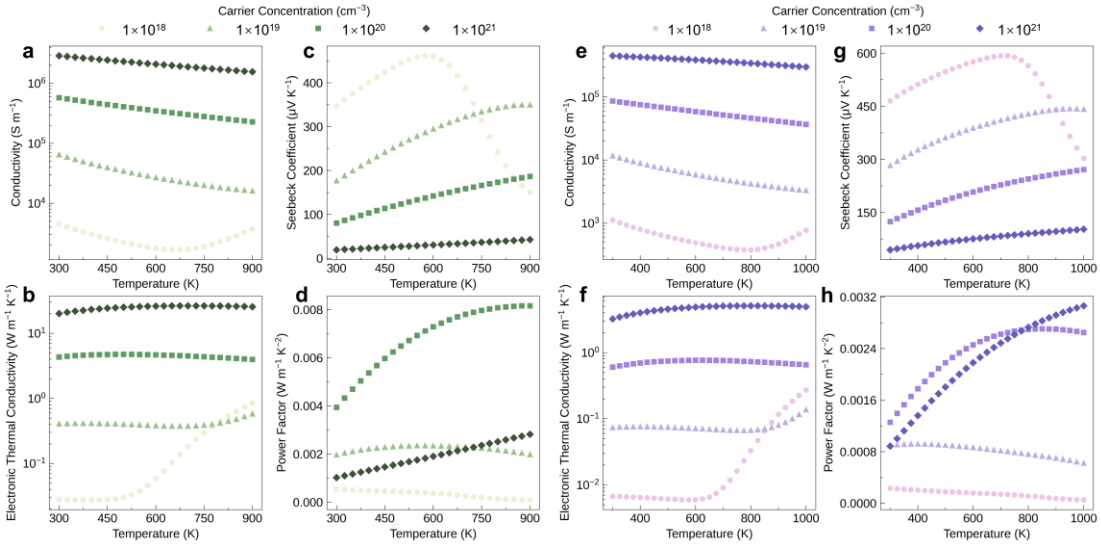

Figure 6 The calculated electronic transport properties as a function of temperature for p-type (a, b, c, and d) $Sb_2Si_2Te_6$ and (e, f, g, and h) $Sc_2Si_2Te_6$ with four different carrier concentrations.

The Seebeck coefficient (S) reflects the voltage generated in response to a temperature gradient, and its sign depends on the dominant charge carrier type (positive for holes, negative for electrons). In general, the Seebeck coefficient can be expressed as:

$$S = \frac{8\pi^2 k_B^2}{3eh^2} m_{DOS}^* T \left(\frac{\pi}{3n}\right)^{\frac{2}{3}} \quad (1)$$

where k_B is the Boltzmann constant, e represents the elementary charge, h denotes Plank's constant, n is the carrier concentration, and m_{DOS}^* represents the DOS effective mass.[23] Thus as witnessed in Figures 5 and 6, the Seebeck coefficient typically exhibits opposite dependence on temperature and carrier concentration compared to the electrical conductivity, decreasing with carrier concentration and increasing with temperature due to their effects on carrier diffusion (and corresponding voltage) across a temperature gradient in a material. For both n and p-type conditions, we see that the Seebeck coefficient in $Sc_2Si_2Te_6$ consistently exceeds that of $Sb_2Si_2Te_6$, showing the opposite behaviour to the electrical conductivity. In particular, n-type $Sc_2Si_2Te_6$ retains

a large Seebeck coefficient (S > 300 μV/K) even at relatively high carrier concentrations (n = 10^{20} cm^{-3}) and electrical conductivities (σ ~ 10^5 S/m). According to equation 1, for a given carrier concentration and temperature, the Seebeck coefficient is primarily determined by the DOS effective mass — which can be approximated by the equation $m_{DOS}^* = N_v^{\frac{2}{3}} m^*$.[24] Here, N_v is the number of degenerate valleys in the electronic band structure and m^* is the effective mass within a single valley. As discussed previously, $Sc_2Si_2Te_6$ exhibits increased band degeneracy (18 and 2 for *n* and *p*-type, respectively, vs 1 for both carrier types in $Sb_2Si_2Te_6$) and carrier effective masses (Table 2) compared to $Sb_2Si_2Te_6$, elucidating the origins of increased Seebeck coefficients for $Sc_2Si_2Te_6$. The calculated electronic transport properties, broken down into the in-plane and cross-plane directions for these layered materials, are provided in the Supplementary Information, with $Sc_2Si_2Te_6$ showing pronounced anisotropy (discussed further below). Additionally, the non-monotonic behaviour for the Seebeck coefficients at low carrier concentrations is due to the bipolar conduction effect, with further discussion provided in the Supplementary Information.

The power factor (PF = $S^2\sigma$) is a key parameter in thermoelectric performance ($ZT \propto$ PF), which can have a complex dependence on carrier concentration and temperature due to their competing effects on S and σ. As a result, a balanced carrier concentration, striking an equilibrium between the Seebeck coefficient and electrical conductivity, is necessary to maximise PF. The optimal PF is higher for p-type (8.16 mW m^{-1} K^{-2}) rather than n-type (4.67 mW m^{-1} K^{-2}) $Sb_2Si_2Te_6$ (Figures 5 and 6). In contrast, for $Sc_2Si_2Te_6$, the highest PF of n-type is 19 mW m^{-1} K^{-2}, which significantly exceeds the value of 3.06 mW m^{-1} K^{-2} for p-type doping (Figures 5 and 6). Moreover, this optimal PF for n-type $Sc_2Si_2Te_6$ markedly exceeds the PF predicted for various layered thermoelectric materials, such as BiCuOSe (~1.71 mW m^{-1} K^{-2}),[13] while it still lags behind that predicted for monolayer SnSe (~28 mW m^{-1} K^{-2}).[25] This ultra-high PF in *n*-type $Sc_2Si_2Te_6$ primarily originates from the enhanced Seebeck coefficient attributable to conduction band degeneracy, as discussed above. Using a band degeneracy strategy to enhance the PF has also been reported in other materials, such as PbTe, which achieves

a band degeneracy of 16 by tuning the doping and composition.[11b]

Thermal transport properties

The calculated lattice thermal conductivity κ_l of both compounds is shown in Figure 7. The lattice thermal conductivity decreases with temperature increases due to greater phonon–phonon scattering at higher temperatures. The lattice thermal conductivity of both compounds is found to be relatively low as expected, particularly in the inter-layer (*z*) direction, with $Sc_2Si_2Te_6$ exhibiting higher lattice thermal conductivity values than $Sb_2Si_2Te_6$ (by a factor of ~3x). This behaviour can be rationalised through the calculated phonon dispersions, which are provided in Figure S8. Given their structural and compositional similarity, the phonon dispersions are relatively similar, with many flat bands present — indicating low phonon group velocities and the likelihood of low lattice thermal conductivity — and the heavy Te atoms dominating the low-energy optical and acoustic modes in both cases. Due to the comparable mass of Sb (121.76 a.u.) and Te (127.60 a.u.) in $Sb_2Si_2Te_6$ (c.f. 44.96 a.u. for Sc), a greater density of phonon bands is witnessed in the low-frequency range (0–5 THz) compared to $Sb_2Si_2Te_6$, leading to increased phonon scattering and thus reduced lattice thermal conductivity as witnessed in Figure 7.

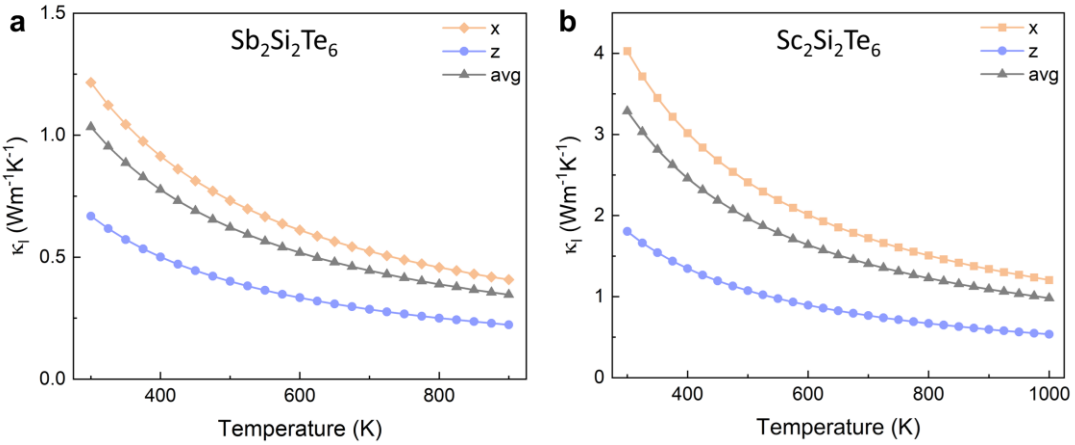

Figure 7 Calculated lattice thermal conductivity κ_l of (a) $Sb_2Si_2Te_6$ and (b) $Sc_2Si_2Te_6$ as a function of temperature. $Sb_2Si_2Te_6$ and $Sc_2Si_2Te_6$ have demonstrated thermal stability up to 920 K and 1023 K,[3a, 7a] respectively, and so these ranges are used in our analysis.

The room temperature lattice thermal conductivity (1.03 W m^{-1} K^{-1}) of $Sb_2Si_2Te_6$ closely aligns with the experimental value (1.0 W m^{-1} K^{-1})[3a] and is also comparable

to that of other layered thermoelectric materials, such as BiCuOSe (1.0 W m^{-1} K^{-1})[13] and Bi_2O_2Se (1.1 W m^{-1} K^{-1}).[26] Importantly, the lattice thermal conductivity is highly anisotropic in both $Sb_2Si_2Te_6$ and $Sc_2Si_2Te_6$, resulting in average $\kappa_{x,y}/\kappa_z$ ratios of 1.82 and 2.24, respectively, at 300 K. The anisotropic nature of lattice thermal conductivity can be attributed to the difference between relatively weak (van der Waals) interlayer interactions along the cross-plane direction and strong (covalent) intralayer interactions along the in-plane direction. Further analysis of the atomistic origins of thermal transport behaviour in these layered compounds was performed by querying the frequency-dependent phonon group velocities, lifetimes and cumulative lattice thermal conductivity, as provided in the Supplementary Information (Figures S9 and S10). These analyses further confirmed the role of Sb/Te mass similarity in the reduced lattice thermal conductivity of $Sb_2Si_2Te_6$, leading to enhanced phonon–phonon scattering and thus reduced phonon lifetimes, rather than any major differences in group velocities.

Thermoelectric figure of merit

With these electrical and thermal transport properties, we can calculate the theoretical dimensionless figure of merit *ZT* for $Sb_2Si_2Te_6$ and $Sc_2Si_2Te_6$ as functions of temperature and carrier concentration (Figures 8 and 9). It is found that for $Sb_2Si_2Te_6$, the p-type system achieves a superior *ZT* compared to the n-type system, while the results are opposite in $Sc_2Si_2Te_6$. For p-type doping, $Sb_2Si_2Te_6$ consistently exhibits higher *ZT* than $Sc_2Si_2Te_6$ regardless of the transport direction, which can be attributed to the lower lattice thermal conductivity (Figure 7) and higher electrical conductivity (Figure 6). However, for *n*-type doping, we find an extremely large calculated *ZT* of 3.51 at 1000 K for the in-plane direction in $Sc_2Si_2Te_6$, greatly surpassing the optimal *ZT* observed (1.69 – 2.06) for n-type $Sb_2Si_2Te_6$. The exceptional *ZT* observed for *n*-type $Sc_2Si_2Te_6$ originates from the dramatically enhanced Seebeck coefficient and PF (Table 4) caused by ultra-high band degeneracy, as discussed above, in combination with the low lattice thermal conductivity (Figure 7). This value surpasses that of typical layered thermoelectric materials, such as p-type SnSe (measured *ZT* of ~ 2.6 at 923 K) and BiCuOSe (predicted *ZT* of 1.32 at 1000 K).[3d, 27] Similar predictions of high *ZT* through

high Seebeck coefficient and PF have also been observed in other materials, such as Na_2TISb ($ZT \sim 4.81$) and InBrSe ($ZT \sim 5.12$).[28] We note that while the in-plane ZT is extremely high for n-type $Sc_2Si_2Te_6$, the cross-plane ZT is very low (0.06 at 1000 K, the ZT without colour scale of n-type $Sc_2Si_2Te_6$ along the cross-plane direction as shown in Figure S11), which can be attributed to the low cross-plane n-type conductivity (Figure S6) — itself a consequence of the relatively localised Sc-d orbitals in the $Sc_2Si_2Te_6$ CBM, giving weak interlayer electronic interactions. Overall, these results suggest that $Sc_2Si_2Te_6$ holds promise as an excellent thermoelectric material for applications in the moderate-to-high temperature range, and also demonstrate the power of band engineering for enhancing thermoelectric performance within compound families. The calculated optimal ZT and associated carrier concentrations, PF, electronic thermal conductivity, and lattice thermal conductivity for $Sb_2Si_2Te_6$ and $Sc_2Si_2Te_6$ are summarized in Tables 3 and 4.

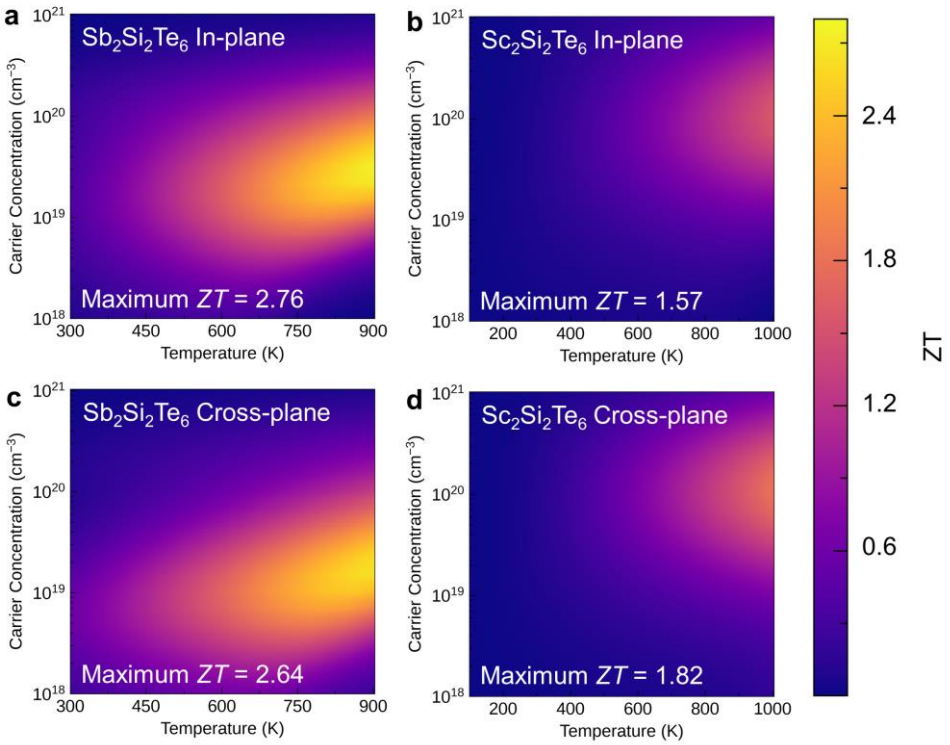

Figure 8 The predicted thermoelectric figure of merit ZT of p-type (a, c) $Sb_2Si_2Te_6$ and (b, d) $Sc_2Si_2Te_6$ against temperature and carrier concentration along the in-plane and cross-plane directions. The lightest colours indicate the highest ZT.

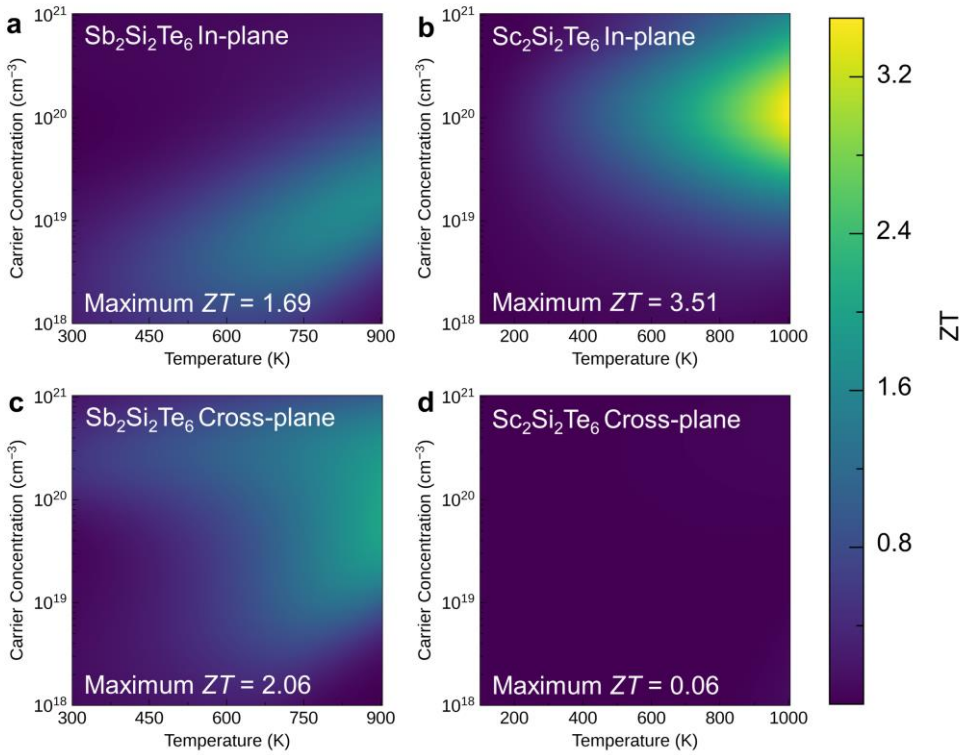

Figure 9 The predicted thermoelectric figure of merit *ZT* of n-type (a, c) $Sb_2Si_2Te_6$ and (b, d) $Sc_2Si_2Te_6$ against temperature and carrier concentration along the in-plane and cross-plane directions. The lightest colours indicate the highest *ZT*.

We note that the theoretically predicted maximum *ZT* for *p*-type $Sb_2Si_2Te_6$ exceeds the experimentally reported result (~1.08 at 823 K, increased to ~1.65 when incorporated in a cellular nanostructure with Si_2Te_3).[3a] Notably, the calculated lattice thermal conductivity of $Sb_2Si_2Te_6$ matches well with the experimental measurements, suggesting the primary origin of reduced *ZT*s in experiment are due to additional scattering mechanisms, for example due to impurities and grain boundaries, and sub-optimal electronic properties such as carrier concentration. This discrepancy can be explained by the following two aspects. On the one hand, in experiment, thermal radiation,[29] air-induced thermal convection[30] impurity phases and the effect of grain boundary scattering on carrier mobility[31] can lead to degradation of thermoelectric performance — effects which are not included in our theoretical model. On the other hand, this experimental value corresponds to a single carrier concentration (measured to be ~5.6×10^{19} cm^{-3} at room temperature) which may vary with temperature, but we calculate the thermoelectric properties over a range of temperatures and carrier

concentrations. Indeed, as expected, we find a high sensitivity of the overall *ZT* to the carrier concentration (Figure 8), with different optimal concentrations for the in-plane and cross-plane directions. Thus, given the un-optimised experimental carrier concentration and potential additional factors not accounted for in our model, a lower experimental figure of merit is expected. Our simulations therefore reflect an idealised model which can help guide experimental efforts in further improving the thermoelectric performance of this material. In particular, the anisotropy in thermoelectric properties indicates that controlled-orientation single crystals (with optimised carrier concentrations) are expected to achieve significantly higher *ZT* values than polycrystalline samples for these layered compounds.

Table 3 Predicted maximum *ZT* in $Sb_2Si_2Te_6$ along the in-plane and cross-plane directions together with corresponding charge carrier concentration (n), power factor (PF), electronic thermal conductivity (κ_e), and lattice thermal conductivity (κ_l).

System	Direction	*ZT*	n (cm^{-3})	PF ($\mu W\ m^{-1}\ K^{-2}$)	κ_e ($W\ m^{-1}\ K^{-1}$)	κ_l ($W\ m^{-1}\ K^{-1}$)
n-type	xy	1.69	1.47×10^{19}	2160	0.70	0.42
	z	2.06	6.81×10^{19}	3520	1.32	0.22
p-type	xy	2.76	3.16×10^{19}	5310	1.32	0.41
	z	2.64	1.47×10^{19}	2120	0.5	0.22

Table 4 Predicted maximum *ZT* in $Sc_2Si_2Te_6$ along the in-plane and cross-plane directions together with corresponding charge carrier concentrations (n), power factor (PF), electronic thermal conductivity (κ_e), and lattice thermal conductivity (κ_l).

System	Direction	*ZT*	n (cm^{-3})	PF ($\mu W\ m^{-1}\ K^{-2}$)	κ_e ($W\ m^{-1}\ K^{-1}$)	κ_l ($W\ m^{-1}\ K^{-1}$)
n-type	xy	3.51	1.16×10^{20}	9110	1.40	1.21
	z	0.06	4.64×10^{20}	30.2	0.014	0.54
p-type	xy	1.57	1.06×10^{20}	3150	0.80	1.21
	z	1.82	1.09×10^{20}	1640	0.37	0.54

Summary

In conclusion, our investigation systematically explored the intrinsic thermoelectric properties of $Sb_2Si_2Te_6$ and $Sc_2Si_2Te_6$, employing a combination of semiclassical Boltzmann transport theory and first-principles calculations. While both layered compounds exhibit low intrinsic lattice thermal conductivities, the low mass difference between Sb and Te results in greater phonon–phonon scattering and shorter phonon lifetimes in $Sb_2Si_2Te_6$, yielding very low lattice thermal conductivity. We find substantial differences in the electronic structures of these two compounds due to the different orbital characters of the A-site cations. Specifically, $Sb_2Si_2Te_6$ manifests a small direct bandgap, while $Sc_2Si_2Te_6$ exhibits a larger, *indirect* bandgap. The combination of crystal (hexagonal ABC stacking) and orbital (hybridized $d_{x^2-y^2}$, d_{xz} and d_{z^2}) symmetry at the $Sc_2Si_2Te_6$ CBM gives rise to a non-high-symmetry band-edge k-point and dramatically enhanced band degeneracy (increasing from 1 in $Sb_2Si_2Te_6$ to 18). Combined with good electron mobility in the in-plane direction, this yields an ultra-high power factor (19 mW m^{-1} K^{-2}) and thus, along with the low lattice thermal conductivity, a large predicted *ZT* of 3.51 for n-type $Sc_2Si_2Te_6$ (compared to the optimal *ZT* of 2.76 for p-type $Sb_2Si_2Te_6$). This enhanced *ZT* arises despite the ~3x increase in lattice thermal conductivity upon substituting Sb with Sc, as the band degeneracy enhancement of the PF overcomes this loss. We note that this optimal *ZT* requires a relatively high charge carrier concentration ($n \sim 10^{20}$ cm^{-3}), so understanding the defect (dopant) chemistry and possible engineering strategies will be key to realising this performance experimentally.[32] This study demonstrates the potential of $Sc_2Si_2Te_6$ for thermoelectric applications and, more broadly, the power of band (degeneracy) engineering as a route to designing high-performance thermoelectric materials.

Supporting Information

Supporting Information is available from the Wiley Online Library or the author.

Acknowledgements

We thank Alex M. Ganose for insightful discussions regarding the electronic band structures of these compounds. W.Z.D, K.B.S, and D.O.S acknowledge support from

the European Research Council (grant 758345). S.R.K. acknowledges the EPSRC Centre for Doctoral Training in the Advanced Characterisation of Materials (EP/S023259/1) for a PhD studentship. W.Z.D and M.Z acknowledge the support of the National Key R&D Program of China (2022YFF0708800), the Natural Science Foundation of Zhejiang Province (LZ22A040004), and the National Natural Science Foundation of China (11674042). W.Z.D acknowledges the support of the international joint doctoral education fund of Beihang University. W.Z.D, K.B.S, S.R.K and D.O.S acknowledge the support of the UCL Myriad and Kathleen High-Performance Computing Facilities (Myriad@UCL, Kathleen@UCL). K.B.S, S.R.K and D.O.S acknowledge the support of the ARCHER2 UK National Supercomputing Service (https://www.archer2.ac.uk) *via* our membership of the UK's HEC Materials Chemistry Consortium, which is funded by the EPSRC (EP/L000202, EP/R029431 and EP/T022213), the UK Materials and Molecular Modelling (MMM) Hub (Young EP/T022213). W.Z.D and M.Z acknowledge the support of the High-Performance Supercomputing Center of Zhongfa Aviation Institute of Beihang University and the Center for High-Performance Computing of Beihang University (BHHPC). K.B.S and D.O.S acknowledge the University of Birmingham's BlueBEAR HPC service (http://www.birmingham.ac.uk/bear); the Baskerville Tier 2 HPC service (https://www.baskerville.ac.uk/), which was funded by the EPSRC and UKRI through the World Class Labs scheme (EP/T022221/1) and the Digital Research Infrastructure programme (EP/W032244/1) and is operated by Advanced Research Computing at the University of Birmingham; and the Sulis Tier 2 HPC platform hosted by the Scientific Computing Research Technology Platform at the University of Warwick, which is funded by EPSRC Grant EP/T022108/1 and the HPC Midlands+ consortium.

Computational Methods

The calculations were performed within density functional theory (DFT) as implemented in the Vienna Ab initio Simulation Package (VASP).[33] The projector augmented wave (PAW) pseudopotential method was employed to account for the interaction between core and valence electrons.[34] A plane-wave kinetic energy cutoff

of 400 eV and a 6×6×6 Γ-centered k-point grid was used for a 10-atom primitive cell, ensuring convergence of total energy within 1 meV/atom using vaspup2.0.[35] The cutoff was increased to 520 eV during geometry optimizations to avoid Pulay stress. To account for Van der Waals dispersion interactions, the D3 correction of Grimme et al. was applied.[35a, 35b] The structures were fully relaxed using the Heyd–Scuseria–Ernzerhof (HSE06) hybrid DFT functional,[36] except for lattice dynamics calculations (ionic contribution to the dielectric constant, polar optical phonon (POP) frequency and phonon force constants) for which the Perdew–Burke–Ernzerhof generalized gradient approximation (GGA) functional for solids (PBEsol) was used.[37] There are no constraints imposed on the unit cell shape or size, and relaxation continued until the change in maximum force on the ions and electronic free energy did not exceed 0.0005 eV/Å and 1×10^{-8} eV, respectively. Electronic structure and high-frequency dielectric constant calculations used HSE06 including spin–orbit coupling (SOC) effects.

The *doped* defect calculation software[15] was used to collate all competing phases in the Sc–Si–Te chemical space within 0.1 eV/atom of the convex hull according to the Materials Project database — which were then re-relaxed and calculated using HSE06+SOC, parse the calculation outputs and plot the calculated chemical stability region (chemical potential ranges) for $Sc_2Si_2Te_6$.

The AMSET software package was employed to calculate the electronic transport properties.[22] Typically, the Boltzmann transport equations are solved using the constant relaxation-time approximation (CRTA), which usually results in the overestimation of *ZT*s.[22, 38] Instead, AMSET improves upon the CRTA by using the momentum relaxation-time approximation (MRTA) to explicitly calculate scattering rates for the individual electronic states within the Born approximation. AMSET offers insights into the contributions to the transport properties from four types of scattering: POP scattering, acoustic deformation potential (ADP) scattering, ionized impurity (IMP) scattering, and piezoelectric (PIE) scattering. These contributions are integrated into the *ZT* equation *via* the electrical conductivity and electronic thermal conductivity. The piezoelectric constant was calculated to be negligible for these materials, and so

piezoelectric scattering is not included in the analysis. The Seebeck coefficient is also calculated by AMSET, but is not influenced by scattering.

The material parameters required as input for AMSET, such as high-frequency and static dielectric constants, elastic constants, phonon frequencies, and deformation potentials, were obtained by first-principles calculations. Ionic dielectric constant contributions and the Γ-point phonon frequencies and dipole moments required to calculate the polar-optic phonon frequency in AMSET were acquired using the finite-displacement method with the PBEsol functional. Deformation potential and high-frequency dielectric constant were determined using HSE06 + SOC. These data are available in Table S1. The transport properties have been converged with respect to the interpolation factor, as shown in Figure S12.

Lattice dynamics calculations were performed using the finite-displacement method within the Phonopy package.[39] Convergence of the phonon dispersion with the supercell size used for second-order force constants (FCs) was explicitly checked, as illustrated in Figure S13. Second-order FCs were computed using a 3×3×1 supercell derived from the 30-atom conventional cell, employing the PBEsol functional.[40] Atom contributions to the lattice dynamics were determined from the atom-projected phonon density of states (PDOS), calculated through Fourier interpolation. The lattice thermal conductivity was calculated using the Phono3py package,[41] which employs a supercell method to calculate the third-order FCs with the PBEsol functional. A 2×2×1 supercell based on the conventional cell was used to calculate the third-order FCs. The lattice thermal conductivity was determined by solving the phonon Boltzmann transport equation within the single-mode relaxation-time approximation. The convergence of q-point mesh density was verified, and a 13×13×13 mesh was selected, as illustrated in Figure S14. Plots of the electronic, phonon and thermoelectric properties were generated using Sumo,[42] IFermi[17] and ThermoParser.[43]

References

[1] G. Tan, L.-D. Zhao, M. G. Kanatzidis, *Chem. Rev.* **2016**, 116, 12123.
[2] a)T. Zhu, Y. Liu, C. Fu, J. P. Heremans, J. G. Snyder, X. Zhao, *Adv. Mater.* **2017**, 29,

1605584; b)Y. Zhou, L. D. Zhao, *Adv. Mater.* **2017**, 29, 1702676.
[3] a)Y. Luo, S. Cai, S. Hao, F. Pielnhofer, I. Hadar, Z.-Z. Luo, J. Xu, C. Wolverton, V. P. Dravid, A. Pfitzner, Q. Yan, M. G. Kanatzidis, *Joule* **2020**, 4, 159; b)Q. Jin, S. Jiang, Y. Zhao, D. Wang, J. Qiu, D. M. Tang, J. Tan, D. M. Sun, P. X. Hou, X. Q. Chen, K. Tai, N. Gao, C. Liu, H. M. Cheng, X. Jiang, *Nat. Mater.* **2019**, 18, 62; c)X. Chen, H. Wu, J. Cui, Y. Xiao, Y. Zhang, J. He, Y. Chen, J. Cao, W. Cai, S. J. Pennycook, Z. Liu, L.-D. Zhao, J. Sui, *Nano Energy* **2018**, 52, 246; d)L. D. Zhao, S. H. Lo, Y. Zhang, H. Sun, G. Tan, C. Uher, C. Wolverton, V. P. Dravid, M. G. Kanatzidis, *Nature* **2014**, 508, 373; e)L. D. Zhao, D. Berardan, Y. L. Pei, C. Byl, L. Pinsard-Gaudart, N. Dragoe, *Applied Physics Letters* **2010**, 97, 092118.
[4] a)M. Samanta, K. Pal, P. Pal, U. V. Waghmare, K. Biswas, *J Am Chem Soc* **2018**, 140, 5866; b)C. Wang, Y. Chen, *npj Computational Materials* **2020**, 6, 26; c)B. Qin, D. Wang, X. Liu, Y. Qin, J.-F. Dong, J. Luo, J.-W. Li, W. Liu, G. Tan, X. Tang, J.-F. Li, J. He, L.-D. Zhao, *Science* **2021**, 373, 556.
[5] a)L. Wu, J. Yang, S. Wang, P. Wei, J. Yang, W. Zhang, L. Chen, *Phys. Rev. B* **2014**, 90, 195210; b)H. Ohta, S. Kim, Y. Mune, T. Mizoguchi, K. Nomura, S. Ohta, T. Nomura, Y. Nakanishi, Y. Ikuhara, M. Hirano, H. Hosono, K. Koumoto, *Nat. Mater.* **2007**, 6, 129.
[6] a)A. Li, C. Hu, B. He, M. Yao, C. Fu, Y. Wang, X. Zhao, C. Felser, T. Zhu, *Nat Commun* **2021**, 12, 5408; b)A. Mehdizadeh Dehkordi, M. Zebarjadi, J. He, T. M. Tritt, *Materials Science and Engineering: R: Reports* **2015**, 97, 1.
[7] a)F. Pielnhofer, S. Bette, R. Eger, V. Duppel, J. Nuss, C. Dolle, R. E. Dinnebier, B. V. Lotsch, *Zeitschrift für anorganische und allgemeine Chemie* **2022**, 648, e202200234 ; b)Y. Luo, Z. Ma, S. Hao, S. Cai, Z. Z. Luo, C. Wolverton, V. P. Dravid, J. Yang, Q. Yan, M. G. Kanatzidis, *J Am Chem Soc* **2022**, 144, 1445; c)M. A. Korkmaz, E. Deligoz, H. Ozisik, *Journal of Electronic Materials* **2021**, 50, 2779; d)I. A. Verzhbitskiy, H. Kurebayashi, H. Cheng, J. Zhou, S. Khan, Y. P. Feng, G. Eda, *Nature Electronics* **2020**, 3, 460; e)C. Gong, L. Li, Z. Li, H. Ji, A. Stern, Y. Xia, T. Cao, W. Bao, C. Wang, Y. Wang, Z. Q. Qiu, R. J. Cava, S. G. Louie, J. Xia, X. Zhang, *Nature* **2017**, 546, 265; f)E. Sandre, V. Carteaux, A. M. Marie, G. Ouvrard, *Journal of Alloys and Compounds* **1994**, 204, 145; g)G. Ouvrard, E. Sandre, R. Brec, *J. Solid State Chem.* **1988**, 73, 27; h)R. E. Marsh, *J. Solid State Chem.* **1988**, 77, 190; i)J. Gopalakrishnan, K. S. Nanjundaswamy, *Materials Research Bulletin* **1988**, 23, 107.
[8] a)D. Yang, W. Yao, Q. Chen, K. Peng, P. Jiang, X. Lu, C. Uher, T. Yang, G. Wang, X. Zhou, *Chem. Mater.* **2016**, 28, 1611; b)R. Lefèvre, D. Berthebaud, O. Lebedev, O. Pérez, C. Castro, S. Gascoin, D. Chateigner, F. Gascoin, *Journal of Materials Chemistry A* **2017**, 5, 19406.
[9] Z. Huang, L.-D. Zhao, *Trends Chem.* **2020**, 2, 89.
[10] a)Y. Pei, J. Lensch-Falk, E. S. Toberer, D. L. Medlin, G. J. Snyder, *Adv. Funct. Mater.* **2011**, 21, 241; b)Q. Zhang, E. K. Chere, Y. Wang, H. S. Kim, R. He, F. Cao, K. Dahal, D. Broido, G. Chen, Z. Ren, *Nano Energy* **2016**, 22, 572; c)C. C. Kang, K. A. Yamauchi, J. Vlassakis, E. Sinkala, T. A. Duncombe, A. E. Herr, *Nat Commun* **2016**, 11, 1508.
[11] a)Y. Pei, H. Wang, G. J. Snyder, *Adv. Mater.* **2012**, 24, 6125; b)Y. Pei, X. Shi, A. LaLonde, H. Wang, L. Chen, G. J. Snyder, *Nature* **2011**, 473, 66; c)C. M. Jaworski, V. Kulbachinskii, J. P. Heremans, *Phys. Rev. B* **2009**, 80, 233201; d)M. Hong, Y. Wang, T. Feng, Q. Sun, S. Xu, S. Matsumura, S. T. Pantelides, J. Zou, Z. G. Chen, *J Am Chem Soc* **2019**, 141, 1742.
[12] a)W. Liu, X. Tan, K. Yin, H. Liu, X. Tang, J. Shi, Q. Zhang, C. Uher, *Phys. Rev. Lett.* **2012**, 108, 166601; b)Y. Dai, W. Zhou, H.-J. Kim, Q. Song, X. Qian, T.-H. Liu, R. Yang, *npj*

Computational Materials **2022**, 8, 234.
[13] N. Wang, M. Li, H. Xiao, Z. Gao, Z. Liu, X. Zu, S. Li, L. Qiao, *npj Computational Materials* **2021**, 7, 18.
[14] a)S. Jaśkaniec, S. R. Kavanagh, J. Coelho, S. Ryan, C. Hobbs, A. Walsh, D. O. Scanlon, V. Nicolosi, *NPJ 2D Mater. Appl.* **2021**, 5, 27; b)I. Maity, P. K. Maiti, M. Jain, *Phys. Rev. B* **2018**, 97, 161406.
[15] S. R. Kavanagh, in *doped Zenodo*, 2023.
[16] W. Setyawan, S. Curtarolo, *Comput. Mater. Sci.* **2010**, 49, 299.
[17] A. M. Ganose, A. Searle, A. Jain, S. M. Griffin, *Journal of Open Source Software* **2021**, 6, 3089.
[18] S.-H. Wei, A. Zunger, *Applied Physics Letters* **1998**, 72, 2011.
[19] J. Nishitani, K. M. Yu, W. Walukiewicz, *Applied Physics Letters* **2014**, 105, 132103.
[20] K. Brlec, K. B. Spooner, J. M. Skelton, D. O. Scanlon, *Journal of Materials Chemistry A* **2022**, 10, 16813.
[21] W.-J. Lee, H. J. Kim, J. Kang, D. H. Jang, T. H. Kim, J. H. Lee, K. H. Kim, *Annual Review of Materials Research* **2017**, 47, 391.
[22] A. M. Ganose, J. Park, A. Faghaninia, R. Woods-Robinson, K. A. Persson, A. Jain, *Nat Commun* **2021**, 12, 2222.
[23] M. Cutler, J. F. Leavy, R. L. Fitzpatrick, *Phys. Rev.* **1964**, 133, A1143.
[24] Z. M. Gibbs, F. Ricci, G. Li, H. Zhu, K. Persson, G. Ceder, G. Hautier, A. Jain, G. J. Snyder, *npj Computational Materials* **2017**, 3, 8.
[25] F. Q. Wang, S. Zhang, J. Yu, Q. Wang, *Nanoscale* **2015**, 7, 15962.
[26] C. Wang, G. Ding, X. Wu, S. Wei, G. Gao, *New J. Phys.* **2018**, 20, 123014.
[27] D. Zou, S. Xie, Y. Liu, J. Lin, J. Li, *Journal of Materials Chemistry A* **2013**, 1, 8888.
[28] a)T. Yue, Y. Zhao, J. Ni, S. Meng, Z. Dai, *npj Computational Materials* **2023**, 9, 17; b)S.-Z. Huang, Q.-Y. Feng, B.-Y. Wang, H.-D. Yang, B. Li, X. Xiang, X.-T. Zu, H.-X. Deng, *ACS Applied Energy Materials* **2022**, 5, 13042.
[29] D. Kraemer, J. Sui, K. McEnaney, H. Zhao, Q. Jie, Z. F. Ren, G. Chen, *Energy & Environmental Science* **2015**, 8, 1299.
[30] Q. Zhu, S. Song, H. Zhu, Z. Ren, *Journal of Power Sources* **2019**, 414, 393.
[31] C. Hu, K. Xia, C. Fu, X. Zhao, T. Zhu, *Energy & Environmental Science* **2022**, 15, 1406.
[32]a)Y. Zheng, T. J. Slade, L. Hu, X. Y. Tan, Y. Luo, Z. Z. Luo, J. Xu, Q. Yan, M. G. Kanatzidis, *Chem Soc Rev* **2021**, 50, 9022; b)P. Gorai, A. Ganose, A. Faghaninia, A. Jain, V. Stevanović, *Mater. Horiz.* **2020**, 7, 1809.
[33] a)G. Kresse, J. Furthmüller, *Phys. Rev. B* **1996**, 54, 11169; b)G. Kresse, J. Furthmiiller, *Comput. Mater. Sci.* **1996**, 6, 15; c)G. Kresse, J. Hafner, *Phys Rev B Condens Matter* **1994**, 49, 14251; d)G. Kresse, J. Hafner, *Phys Rev B Condens Matter* **1993**, 47, 558.
[34] a)G. K. a. D. Joubert, *Phys. Rev. B* **1999**, 59, 1758; b)P. E. Blochl, *Phys Rev B Condens Matter* **1994**, 50, 17953.
[35] a)S. Grimme, S. Ehrlich, L. Goerigk, *J Comput Chem* **2011**, 32, 1456; b)S. Grimme, J. Antony, S. Ehrlich, H. Krieg, *J. Chem. Phys.* **2010**, 132, 154104; c)S. R. Kavanagh, in *vaspup2.0 Zenodo*, vaspup2.0 Zenodo 2023.
[36] a)A. V. Krukau, O. A. Vydrov, A. F. Izmaylov, G. E. Scuseria, *J. Chem. Phys.* **2006**, 125, 224106; b)J. Heyd, G. E. Scuseria, M. Ernzerhof, *The Journal of Chemical Physics* **2003**, 118,

8207.
[37] a)J. P. Perdew, K. Burke, M. Ernzerhof, *Phys. Rev. Lett.* **1996**, 77, 3865; b)J. P. Perdew, A. Ruzsinszky, G. I. Csonka, O. A. Vydrov, G. E. Scuseria, L. A. Constantin, X. Zhou, K. Burke, *Phys. Rev. Lett.* **2008**, 100, 136406.
[38] K. B. Spooner, A. M. Ganose, W. W. W. Leung, J. Buckeridge, B. A. D. Williamson, R. G. Palgrave, D. O. Scanlon, *Chem. Mater.* **2021**, 33, 7441.
[39] A. Togo, I. Tanaka, *Scripta Materialia* **2015**, 108, 1.
[40] J. M. Skelton, D. Tiana, S. C. Parker, A. Togo, I. Tanaka, A. Walsh, *The Journal of Chemical Physics* **2015**, 143, 064710.
[41] A. Togo, L. Chaput, I. Tanaka, *Phys. Rev. B* **2015**, 91, 094306.
[42] A. M. Ganose, A. J. Jackson, D. O. Scanlon, *Journal of Open Source Software* **2018**, 3, 717.
[43] K. B. Spooner, M. Einhorn, D. W. Davies, D. O. Scanlon, in *ThermoParser: Streamlined Analysis of Thermoelectric Properties*, https://github.com/SMTG-Bham/ThermoParser 2023.

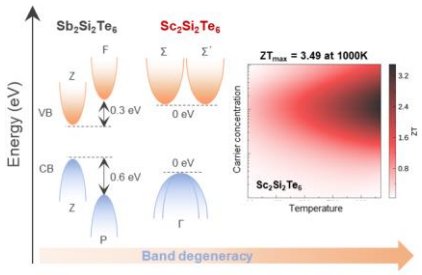

The Sc element significantly increases the conduction band degeneracy and thus the Seebeck coefficient in $Sc_2Si_2Te_6$ compared to $Sb_2Si_2Te_6$. As a result, a compelling *ZT* of 3.51 is achieved in n-type $Sc_2Si_2Te_6$, exceeding the optimal *ZT* of 2.76 in p-type $Sb_2Si_2Te_6$ 27 %.